International Journal of ISSI, Vol.11 (2014), No.2, pp. 1-5

Austenite Stability during Nanoindentation of Ultrafine and Coarse Grained AISI 304L Stainless Steels

S.Sabooni [1], Z.Aghaei [2], F.Karimzadeh [3], M.H.Enayati [4], A.H.W.Ngan [5]*
[1,2,3,4] Department of Materials Engineering, Isfahan University of Technology, 84156-83111, Isfahan, Iran
[5] Department of Mechanical Engineering, The University of Hong Kong, Pokfulam Road, Hong Kong, China

Abstract

In the present study, the effect of grain size on the austenite stability was studied by nanoindentation tests in a 304L stainless steel. Thermomechanical processing based on cold rolling and annealing was used to produce two different types of austenite: ultrafine grained (UFG) austenite with the average grain size of 0.65 μm and coarse grained (CG) austenite with the average grain size of 12 μm. Scanning Electron Microscope (SEM) and Transmission Electron Microscope (TEM) were used to follow the microstructural changes during rolling and annealing. The results of nanoindentation tests showed pop-in in the load-displacement curve of the CG sample while no observable pop-in was found in the UFG sample. The slope of (P/h) versus h plot, where P was load and h was displacement, was changed after the occurrence of each pop-in event in the CG sample. This behavior was related to the change of plastic deformation mode due to the martensitic transformation. The present results, therefore, confirmed that the UFG austenite had higher stability to withstand martensitic transformation.

Keywords: Nanoindentation, Martensitic transformation, Austenitic stainless steel, Pop-in.

1. Introduction

It is well known that austenite can be transformed into martensite above the martensite-start temperature (Ms) by mechanical deformation [1]. In recent years, thermomechanical treatment based on Strain Induced Martensitic Transformation (SIMT) and reverse annealing has attracted a lot of attention in the fabrication of ultrafine grained (UFG)/nano grained (NG) stainless steels [2-5].The UFG/NG stainless steels produced by this method normally show a good combination of strength and elongation due to the increased strain-hardening rate [2-5]. The transformation of austenite to martensite during mechanical loading depends on different parameters such as temperature, alloy chemical composition, strain rate and grain size. Among these parameters, the austenite grain size is much more important because its reduction can improve the austenite stability and retard strain induced martensitic transformation. For example, Varma et al. [6] investigated the effects of austenite grain size ranging from 52 μm to 200 μm on the martensite formed during tensile tests, confirming that the volume of SIMT was increased with increasing austenite grain size. Although some works have been carried out regarding the effects of grain size on the stability of austenite in stainless steels, most of them have been limited to the micron range of grain sizes produced by conventional processing routes [6]. It is, therefore, interesting to know whether such a behavior remains in the UFG region or not. Nanoindentation testing has a lot of advantages, and, in particular, it is useful for investigating the onset of deformation. The indentation of austenite has been reported to create high stresses which can cause martensitic transformation in high manganese stainless steels [7-9]. Ahn et al.[7] studied strain induced martensitic transformation during the nanoindentation of individual grains in a Fe–0.08C–0.5Si–1Al–7Mn (wt.%) transformation induced plasticity (TRIP) steel. They found that the observed pop-in in the load-displacement curve of indentation was due to the geometrical softening accompanying the selection of favorable martensite variants based on the mechanical interaction energy between the externally applied stress and lattice deformation during nanoindentation. Sekido et al. [8] reported that the martensitic transformation induced by nanoindentation produced ε-martensite with HCP structure, rather than α/ martensite with BCC structure, in a Fe-28Mn-6Si-5Cr alloy. He et al. [9] also studied the effect of Mn content on

** Corresponding author*
Email: s.sabooni@ma.iut.ac.ir
Address: Department of Materials Engineering, Isfahan University of Technology, 84156-83111, Isfahan, Iran
1. PhD Student
2. BSc
3. Associate Professor
4. Professor
5. Professor

the stability of retained austenite during nanoindentation and found that the higher Mn content resulted in higher stability during indentation. As reviewed in the literature, most of the published work regarding austenite stability during nanoindentation has been limited to TRIP steel and/or high Mn steels. Therefore, the aim of the present work was to compare the austenite stability of UFG and a CG 304L stainless steel during nanoindentation tests.

2. Materials and Methods

The starting material was a commercial AISI 304L stainless steel plate with the thickness of 10 mm. Table 1 presents the chemical composition of the studied stainless steel. SEM micrograph of the as-received material is shown in Fig. 1. The as-received microstructure consisted of austenite grains with the average grain size of 35 μm and delta ferrite precipitates. The as-received material was subjected to multipass unidirectional rolling up to 80% rolling reduction at the temperature of -15 ^{o}C. Changes in martensite area fraction during cold rolling were evaluated using ferritescope. The cold rolled specimens were annealed at 700 ^{o}C and 900 ^{o}C for 5h and 3h respectively. This was to obtain UFG and CG austenite with the grain size of 0.65 μm and 12 μm, respectively. The samples were mechanically ground using grinding papers from 80 to 4000 grits and then polished with alumina slurry. The samples were then electro-polished using an electrolytic bath of 200 mL $HClO_4$ and 800 mL ethanol before the nanoindentation tests. Nanoindentation experiments were carried out in the load control mode with the maximum load of 1 mN using an Agilent G200 machine equipped with a Berkovich tip. 25 indentations were performed on each sample and the average hardness and elastic modulus were reported. High Resolution Scanning Electron Microscope, Electron back scattered diffraction (EBSD) and Transmission Electron Microscope were used to characterize the microstructure of the ultrafine and coarse grained steels.

Table 1. Chemical composition of AISI 304L stainless steel used in this investigation.

element	C	Cr	Ni	Mo	Mn	Si	P	S	Co	Cu	V	Fe
wt.%	0.026	18.35	8.01	0.15	1.24	0.323	0.024	0.005	0.129	0.24	0.1	Remain

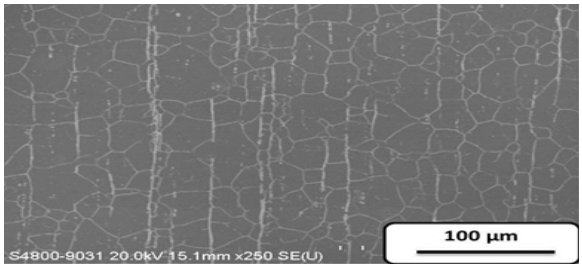

Fig.1. SEM micrograph of the as-received 304L stainless steel.

3. Results and Discussion

Fig. 2(a) shows the amount of deformation induced martensite during rolling vs true strain (ε = ln (1/1-r)) in the rolling process. Increasing the rolling reduction caused the transformation of austenite to deformation induced martensite. It can be seen that the transformation curve had a sigmoidal shape. The Olsen-Cohen equation [10] was used to fit the experimental data of martensite fraction versus true strain:

$$f^{\alpha'} = 1 - \exp\left\{-\beta\left[1 - \exp\left(-\alpha\varepsilon\right)\right]^{n}\right\} \qquad \text{(Eq. 1)}$$

where α and β are temperature dependent constants and n is equal to 4.5. The α parameter mainly depends on the stacking fault energy of the steel and β is related to the possibility of the nucleation of an α′ nucleus at a shear band intersection. After fitting, the values of α and β were calculated to be 6.077 and 2.966. Martensite area fraction was plotted using fitted Olsen-Cohen equation as shown in Fig. 2(a). The Olsen-Cohen equation is a nucleation-controlled model, assuming that the controlling factor in martensitic transformation kinetics is nucleation based. Therefore, a good agreement of the experimental data with this equation suggests that martensitic transformation occurs based on the nucleation and growth of martensite. Fig. 2(b) shows a TEM micrograph of the 5% cold rolled sample. Martensite nuclei could be seen clearly in the intersections between the shear bands. The Selected Area Diffraction (SAD) pattern in Fig. 2(c) consists of a strong set of diffraction spots which represent the FCC structure of austenite and a pale set of spots which show the BCC structure of α′ martensite. No sign of ε martensite with HCP crystal structure was found in the SAD pattern. It has been reported that the shear bands produced during deformation are the main sites for the nucleation of martensite [11-13]. Increasing the rolling reduction caused an increase in the amount of deformation induced martensite so that after 35 % reduction (ε = 0.43), 84 % of the matrix was covered with martensite (Fig. 2(c)), and, after 55% rolling reduction, almost all of the matrix (more than 98%) was covered with deformation induced martensite. TEM micrograph of the 60% rolled sample is shown in Fig. 2(d), confirming that the matrix was fully covered with deformation induced martensite with lathe width being around 100 nm. Further rolling up to 80% decreased the widths of the lathes and increased the amount of dislocations which acted as the nucleation sites for obtaining the UFG structure during the reversion annealing treatment [14-15].

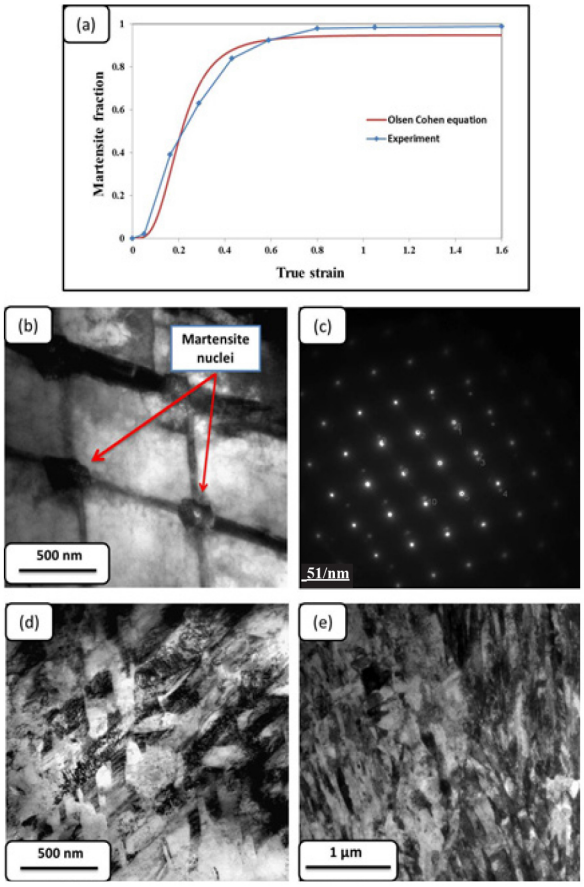

Fig. 2. Martensite area fraction versus true strain during cold rolling (a), TEM micrograph and related SADP of the rolled samples after (b and c) 5%, (d) 35%, and (e) 60 % reduction.

Different annealing conditions were applied to the 80% cold rolled sample for the reversion treatment of martensite to obtain austenite with different grain sizes. Fig. 3 shows the SEM and TEM micrographs of a UFG (Fig.3 (a and b)) and a CG sample (Fig.3 (c and d)), with an average grain size of 0.65 µm and 12 µm, respectively. It should be noted that the dark precipitates in the samples were delta ferrite. Fig. 4 shows the EBSD analysis of the coarse grained sample. Black, red and green colors represent the high angle grain boundaries (HAGBs), low angle grain boundaries (LAGBs) and Σ3 boundaries, respectively. Also, the blue color indicates delta ferrite particles distributed in the matrix. The results of EBSD analysis showed that the amount of delta ferrite in the matrix was less than 2%, which was much lower than the 7% in the coarse grained sample, possibly due to the higher annealing temperature for the CG sample, which could promote the dissolution of delta phase in the matrix. It should be noted that the amount of delta ferrite in the UFG sample was evaluated using image analysis of SEM images. This was because the existence of a high fraction of grain boundaries in the UFG sample increased the zero solution points of the EBSD analysis, which finally decreased the quality of the micrograph. Misorientation angle distribution presented in Fig. 4(b) also showed that a large fraction of boundaries were high angle, especially Σ3 in nature. These Σ3 boundaries were annealing twins produced during the high temperature annealing of the CG sample. In addition, the higher temperature during the annealing of CG sample resulted in lower dislocation density of the austenite phase.

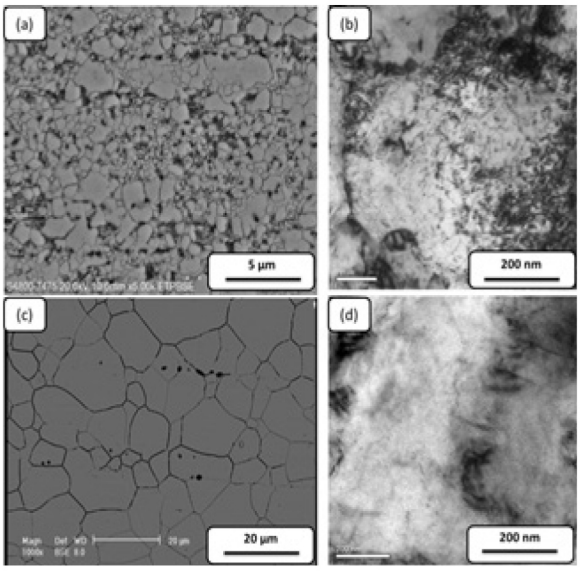

Fig. 3. SEM and TEM micrographs of the (a and b) UFG sample and (c and d) CG sample.

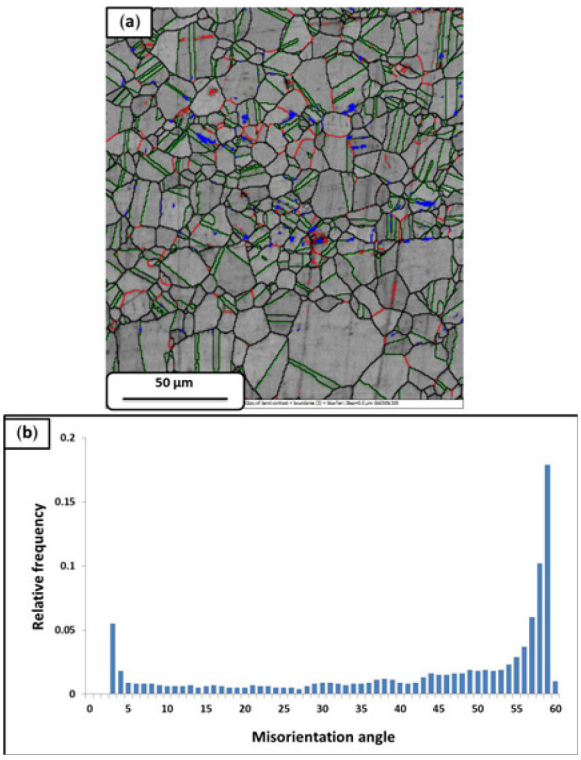

Fig. 4. EBSD Analysis of the coarse grain sample (a) boundaries Map and (b) Misorientation angle distribution.

Fig. 5 shows the load-displacement curves of the CG and UFG samples under the same loading profile. The average hardness of the UFG sample and that of the CG sample were calculated as 7 GPa and 5 GPa, respectively. Meanwhile, the elastic modulus of both samples was calculated to be around 210 GPa, showing that the elastic modulus was not influenced noticeably by the grain size in the range studied. This is consistent with previous studies concluding that the elastic modulus of nanostructured iron is the same as that of coarse grained iron, except that the grain size becomes smaller than 20 nm [16]. The higher measured hardness of the UFG sample, in comparison with the CG counterpart, was not unexpected due to the lower grain size and the higher dislocation density of the UFG sample. Two discontinuities (pop-in events) could be seen clearly in the load-displacement curve of the CG sample, at the normal loads of 0.15 mN and 0.56 mN, respectively. Meanwhile, similar pop-in events were not observed from the UFG sample.

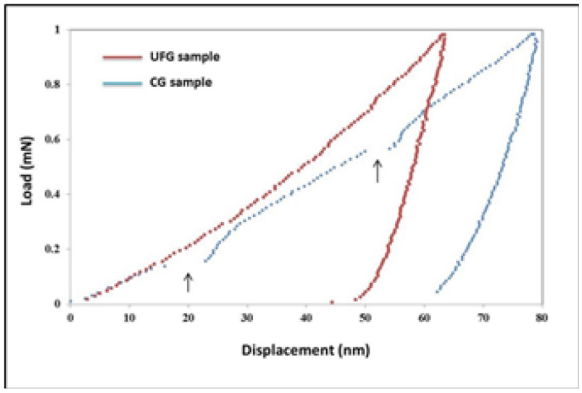

Fig. 5. Load – displacement curve during the nanoindentation of UFG and CG samples. Pop-in events in the CG sample are indicated by arrows.

The experimental load-displacement curve of the CG sample was compared with the calculated behavior based on the Hertzian elastic contact theory [17] (Fig.6 (a)). By assuming that the indenter is spherical at shallow depths, the Hertzian solution [17] gives:

$$P = \frac{4}{3} E_r R_i^{1/2} h^{3/2} \qquad \text{(Eq. 2)}$$

where P is the applied load, E_r is the effective indentation modulus, R is the radius of the indenter tip and h is the penetration depth. The end-radius of a new Berkovich tip is normally between 50-100 nm, which is usually increased to 200 nm or beyond after usage. Here, 200 nm was used as the tip radius. The effective indentation modulus is related to the Young modulus and Poisson ratio of the sample (E_s = 210 GPa, υ_s = 0.3) and indenter (E_i = 1140 GPa, υ_i = 0.07) according to the following relation:

$$\frac{1}{E_r} = \frac{1-\upsilon_i^2}{E_i} + \frac{1-\upsilon_s^2}{E_s} \qquad \text{(Eq. 3)}$$

Where the subscripts i and s refer to the indenter and sample, respectively. As can be seen from Fig. 5(a), the elastic portion of the experimental curve was fitted with the obtained Hertzian curve very well, implying that the assumption of 200 nm for the tip radius tip was reasonable. The Hertzian curve, however, departed from the experimental curve at the depth of about 7 nm, which was lower than the load at which the first pop-in occurred. So it was clear that the first pop-in could not be due to the dislocation nucleation accompanying the start of plastic deformation. The (P/h) versus h curve was plotted from the experimental load displacement in order to gain more insights into the pop-in events. In the fully elasto-plastic regime, the theoretical load applied with a conical or pyramidal indenter should be a parabolic function of depth [17], i.e.

$$P_t = bh^2 \qquad \text{(Eq. 4)}$$

Where b is a material constant that depends on the elastic properties and the plastic hardness of the material. Therefore, for full elasto-plastic deformation, the (P/h) versus h plot should show a constant slope equal to b in Eq. (4). In addition, the spring force due to the stiffness of load frame should also contribute to the measured load. So Eq. 4 should be modified into:

$$P_m = ah + bh^2 \qquad \text{(Eq. 5)}$$

Where a is a constant depending on the shape of the indenter and stiffness of the load frame. It should be noted that the mentioned parameter shows itself as y-intercept in the (p/h) versus h plot and does not have any effect on the curve slop. Considering the fact that the deformation during indentation consists of both elastic and plastic components which may be assumed to be in series, Eqn. (4) can be written as:

$$P_t = b_e h_e^2 = b_p h_p^2 = bh^2 \qquad \text{(Eq. 6)}$$

Where b_e and b_p are constants for the elastic and plastic components. b_p is proportional to the hardness ($H = \frac{P}{Ac}$). Since h can be written as the simple addition of h_e and h_p [18], the relationship between b, b_e and b_p is given by:

$$b^{-1/2} = b_e^{-1/2} + b_p^{-1/2} \qquad \text{(Eq. 7)}$$

With the assumption that b_e is not affected by plastic deformation, b_p can be the only factor controlling the slope of the (P/h) versus h plot. As a result, the change in deformation mode can exhibit itself

as a change in the slope of (P/h) versus h plot. Fig .6 (b) shows the (P/h) versus h plot of the coarse grained sample. The occurrence of successive pop-ins here cannot be explained satisfactorily by dislocation nucleation from an initial dislocation-free state, since after dislocations are generated from a first pop-in, there may be no reason for the occurrence of a second one. Before the first pop-in, the slope of the curve was 0.046 $\mu N/nm^2$, which was increased to 0.6 $\mu N/nm^2$ after the first pop-in, and this trend was repeated in the second pop-in, where the slope of the curve was increased from 0.049 $\mu N/nm^2$ before the pop-in to the 0.5 $\mu N/nm^2$. This behavior of the pop-ins and their successive occurrence can be better explained by martensitic transformation followed by strain hardening. Since martensitic transformation is a nucleation-controlled transformation which occurs at rather high speeds, the indenter tip will be displaced rapidly as the strain induced transformation occurs in order to maintain a constant loading rate in the load control mode, leading to a pop-in. TEM observations of previous studies reviewed in the literature can also prove this kind of transformation during nano-indentation [8-9]. For the UFG sample, no observable pop-in was found in the load-displacement curve. This behavior can confirm that as the grain size of the austenite is decreased, the stability of austenite against martensitic transformation is increased.

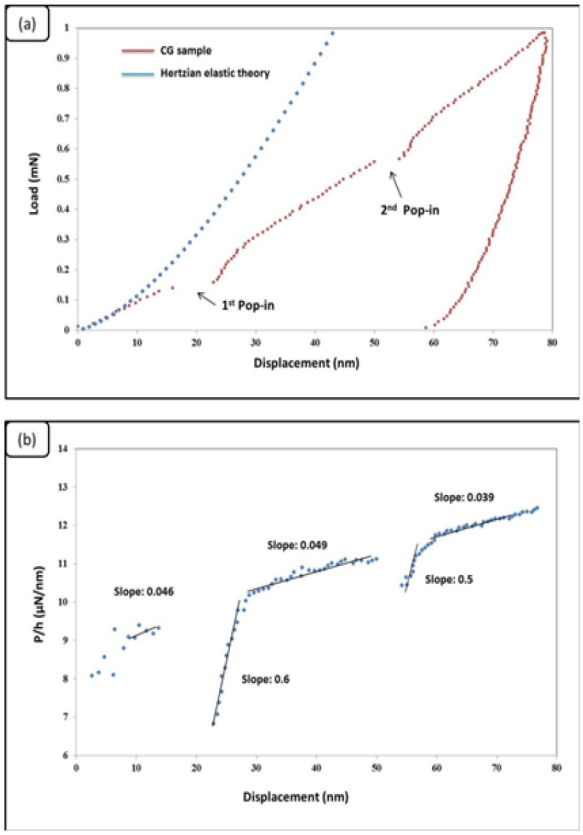

Fig. 6. (a) Load-displacement curve of the CG sample with Hertzian elastic solution (arrows indicate the positions of the pop-in events), and (b) The (P/h) versus h plot (solid lines indicate the slope of the curve).

4. Conclusion

In the present study, martensite thermomechanical processing was used to produce a UFG and a CG steel with the average grain size of 0.65 μm and 12 μm, respectively. Nanoindentation tests were then carried out to study the effects of grain size on the austenite stability during indentation. The load-displacement curve of the CG sample contained pop-in events while no observable pop-in was found in the UFG sample. Analysis of the slope of the (P/h) versus h plot showed that the plastic deformation mechanism was changed during each pop-in. Since martensitic transformation was a nucleation-controlled transformation occurring at high speeds, a pop-in resulted in the load-controlled mode. This study confirmed that reducing the grain size led to higher austenite stability.

References

[1] J.R. Davis, ASM Specialty Handbook: Stainless Steel, Met al.s Park, OH, 1994.
[2] V.S.A. Challa, X.L. Wan, M.C. Somani, L.P. Karjalainen, R.D.K. Misra: Mater. Sci. Eng A., 613 (2014), 60.
[3] R.D.K. Misra, S. Nayak, S.A. Mali, J.S. Shah, M.C. Somani, L.P. Karjalainen: Metall. Mat. Trans. A., 41(2010), 3.
[4] S. Rajasekhara, P.J. Ferreira, L.P. Karjalainen, A. Kyröläinen: Metall. Mat. Trans A., 38 (2007), 202.
[5] A. Momeni, S.M. Abbasi: J. Mater. Sci. Technol., 27 (2011), 338.
[6] S. K. Varma, J. Kalyanam, L. E. Murk, V. Srinivas: J. Mater. Sci. Lett., 13(1994), 107.
[7] T.H. Ahn, C.S. Oh, D.H. Kim, K.H. Oh, H. Bei, E.P. George, H.N. Han: Scripta mat., 63 (2010), 540.
[8] K. Sekido, T. Ohmura, T. Sawaguchi, M. Koyama,H.W. Park , K. Tsuzaki, Scripta mat., 65(2011), 942.
[9] B.B. He, M.X. Huang, Z.Y. Liang, A.H.W. Ngan, H.W. Luo, J. Shi, W.Q. Cao and H. Dong: Scripta Mat., 69 (2013), 215.
[10] G.B. Olsen., M. Cohen: Metall. Mat. Trans. A., 6 (1975), 791.
[11] K.H. Lo , C.H. Shek, J.K.L. Lai: Mater. Sci. Eng R., 65 (2009), 39.
[12] T. Kruml, J. Polak, S. Degallaix: Mater. Sci. Eng A., 293 (2000), 275.
[13] C.X. Huang, G. Yang, Y.L. Gao, S.D. Wu, S.X. Li: J. Mater. Res., 22 (2007), 724.
[14] S. Takaki, K. Tamimura, S.Ueda: ISIJ International., 34 (1994), 522.
[15] R.D.K. Misra, S. Nayak, S.A. Mali, J.S. Shah, M.C. Somani, L.P. Karjalainen: Metall. Mat. Trans. A., 40(2009), 2498.
[16] C. P. Poole, F.J. Owens, Introduction to nanotechnology, Wiley Interscience publication, 2003.
[17] K.L. Johnson, Contact mechanics, Cambridge university press, Cambridge, 1985.
[18] W.C. Oliver, G.M. Pharr: J. Mater. Res., 7 (1992), 1564.